A quasi-backscattering problem for inverse acoustic scattering in the Born regime

Houssem Haddar, Jacob Rezac

A quasi-backscattering problem for inverse acoustic scattering in the Born regime

Houssem Haddar[1] **and Jacob D Rezac**[2]

[1]INRIA Saclay Ile de France/CMAP Ecole Polytechnique, Route de Saclay, 91128 Palaiseau Cedex, France
[2]Department of Mathematical Sciences, University of Delaware, Newark, DE 19716, USA

E-mail: houssem.haddar@inria.fr, jrezac@udel.edu

Abstract. We consider the problem of detecting three-dimensional inclusions from quasi-backscattering far field data generated by an incident field of time-harmonic fixed frequency plane waves modeled with the Born approximation. We assume only partial far field data is known and use a sampling-type method to reconstruct small obstacles and extended spherical obstacles. In particular, at the location of a device transmitting an incident wave, we assume far field data is collected only along a line extending a short distance from the transmitting device. Several numerical examples are provided to demonstrate the effectiveness of the approach.

1. Introduction

In this paper we propose a data collection geometry in which to frame the inverse scattering problem of locating unknown obstacles from far field measurements of time-harmonic scattering data. The measurement geometry, which we call a quasi-backscattering set-up, requires less data than traditional multi-static configurations. We demonstrate that the data collected can be used to locate inhomogeneities whose physical properties are such that the Born approximation applies. In particular, we are able to image a two-dimensional projection of the location of a small obstacle by checking if a test function which corresponds to a point in $\mathbb{R}^2$ belongs to the range of a measurable operator. Combining several projections then allows us to identify the location of the small inclusions in $\mathbb{R}^3$. We also show how this algorithm can be extended to the case of extended spherical inclusions.

Our reconstruction algorithm uses ideas from sampling-type methods [3, 13, 9, 6] and MUSIC-type (MUltiple-SIgnal-Classification) algorithms for small obstacles as in [8, 10, 12, 1, 2, 11]. However, the data setting and analysis are different. Typical scattering experiments collect either backscattering data, in which one device acts as both transmitter and receiver, or multi-static data, in which many transmitting/receiving devices surround the inhomogeneity. The algorithms in the above-mentioned references work only for multi-static data. The inversion scheme we describe in this paper makes use of a type of quasi-backscattering data; one device acts as a transmitter and a line of receivers extends in one-dimension a small distance from the transmitter. Figure 1 demonstrates the difference between a usual multi-static

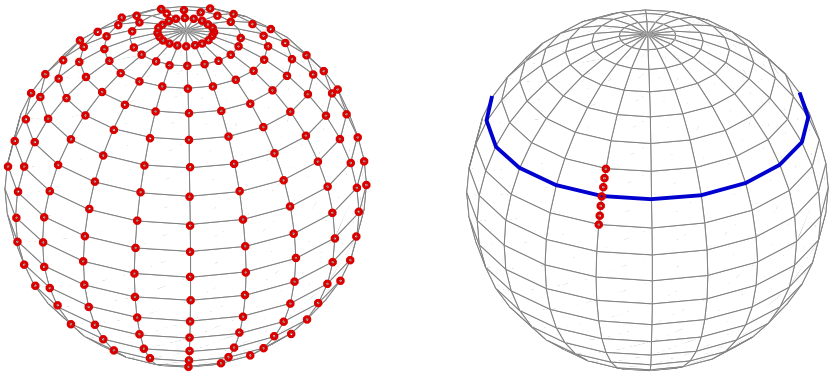

Figure 1: A Comparison of multi-static data (left) and quasi-backscattering data (right). Red circles correspond to device locations. The thick blue line in the right figure denotes where the quasi-backscattering set-up is moved and where each transmitting device is located.

set-up and the quasi-backscattering geometry. As the figure demonstrates, the quasi-backscattering geometry requires significantly less data than the multi-static geometry, which can be beneficial in practical applications. While the proposed scheme can be applied to other types of problem, we focus here on the inverse acoustic scattering problem.

The outline of our paper is as follows: in Section 2, the direct scattering problem is formulated and the quasi-backscattering data setting is explicated. In Section 3, we introduce and analyze the inversion procedure capable of identifying two-dimensional projections of small objects' locations. We then extend the algorithm to the case of extended spherical inclusions. In Section 4, extensive numerical experimentations are presented in order to show the performance of this new algorithm. We end this section by explaining how one can obtain three-dimensional locations from two-dimensional projections.

2. Direct scattering problem

We begin by discussing the mathematical formulation for the problem of acoustic incident plane waves scattering against inhomogeneous media in three-dimensions. These details can be found in many places, e.g. [7], and we include them here for completeness.

Assume a plane wave incident field with a fixed wave number k is generated in the area of an inhomogeneity. Such an incident field is described by $u^i(\mathbf{x}, \hat{\mathbf{d}}) = e^{ik\hat{\mathbf{d}}\cdot\mathbf{x}}$ for $\mathbf{x} \in \mathbb{R}^3$ and $\hat{\mathbf{d}} \in \mathbb{S}^2$ where $\mathbb{S}^2$ is the boundary of the unit ball in $\mathbb{R}^3$ and where $\hat{\cdot}$ indicates a normalized vector. The total field $u(\mathbf{x})$ satisfies

$$\Delta u + k^2 n(\mathbf{x}) u = 0 \quad \text{in} \quad \mathbb{R}^3, \tag{1a}$$

$$u(\mathbf{x}) = u^i(\mathbf{x}, \hat{\mathbf{d}}) + u^s(\mathbf{x}), \tag{1b}$$

$$\lim_{r\to\infty} r\left(\frac{\partial u^s}{\partial r} - iku^s\right) = 0, \tag{1c}$$

where $u^s(\mathbf{x})$ is the scattered field, $r = |\mathbf{x}|$ is the Euclidean magnitude of $\mathbf{x}$, $n(\mathbf{x})$ is

the refractive index of the inhomogeneous medium which is a bounded function with non-negative imaginary part, and $(1c)$ is the Sommerfeld radiation condition which holds uniformly with respect to $\hat{\mathbf{x}} = \mathbf{x}/|\mathbf{x}|$. For wave numbers such that $\mathrm{Im}k \geq 0$ and refractive indices which are bounded with compact support, it is known that $(1a)$–$(1c)$ has a unique solution in $H^1_{\mathrm{loc}}(\mathbb{R}^3)$. This problem has been studied extensively and more information about the related direct and inverse problems can be found in, e.g., [3, 7, 13].

In what follows, define the contrast function as $m(\mathbf{x}) = 1 - n(\mathbf{x})$ and assume $m(\mathbf{x})$ is non-zero only on a compact set $D \subset \mathbb{R}^3$ which contains the inhomogeneity. The Lippmann-Schwinger equation,

$$u(\mathbf{x}) = e^{ik\mathbf{x}\cdot\hat{\mathbf{d}}} - k^2 \int_D m(\mathbf{y})\Phi(\mathbf{x},\mathbf{y})u(\mathbf{y})\,\mathrm{d}\mathbf{y}, \tag{2}$$

gives an exact expression for the unique solution to $(1a)$-$(1c)$ where

$$\Phi(\mathbf{x},\mathbf{y}) = \frac{1}{4\pi}\frac{e^{ik|\mathbf{x}-\mathbf{y}|}}{|\mathbf{x}-\mathbf{y}|}, \qquad \mathbf{x} \neq \mathbf{y}$$

is the fundamental solution to the Helmholtz equation in $\mathbb{R}^3$. Assuming [13] $k^2 \max_{\mathbf{x}\in\overline{D}} \int_D |m(\mathbf{y})\Phi(\mathbf{x},\mathbf{y})|\,\mathrm{d}y \ll 1$, the first term of a Neumann series solution to (2) gives the Born approximation

$$u^B(\mathbf{x}) = e^{ik\mathbf{x}\cdot\hat{\mathbf{d}}} - k^2 \int_D m(\mathbf{y})\Phi(\mathbf{x},\mathbf{y})e^{ik\hat{\mathbf{d}}\cdot\mathbf{y}}\,\mathrm{d}\mathbf{y}. \tag{3}$$

The inverse problem in which we are interested is to find information about D given data about the asymptotic behavior of $u^s_B(\mathbf{x})$, the Born approximation to the scattered field. We are able to explicitly characterize the asymptotic behavior of the scattered field through the Sommerfeld radiation condition, $(1c)$. Specifically,

$$u^s_B(\mathbf{x}) = \frac{e^{ik|x|}}{|x|}u^B_\infty(\hat{\mathbf{x}},\hat{\mathbf{d}}) + O\left(\frac{1}{|x|^2}\right), \qquad |\mathbf{x}| \to \infty$$

where $u^\infty_B(\hat{\mathbf{x}},\hat{\mathbf{d}})$ is the Born approximation to what is known as the far field pattern. Using (3),

$$u^s_B(\mathbf{x}) = -k^2 \int_D m(\mathbf{y})\Phi(\mathbf{x},\mathbf{y})e^{ik\hat{\mathbf{d}}\cdot\mathbf{y}}\,\mathrm{d}\mathbf{y}$$

and we conclude that

$$u^B_\infty(\hat{\mathbf{x}},\hat{\mathbf{d}}) = -\frac{k^2}{4\pi}\int_D e^{ik(\hat{\mathbf{d}}-\hat{\mathbf{x}})\cdot\mathbf{y}}m(\mathbf{y})\,\mathrm{d}\mathbf{y}, \qquad \hat{\mathbf{x}} \in \mathbb{S}^2. \tag{4}$$

2.1. Forward problem for quasi-backscattering data

The above derivations have not fixed the measurement geometry. We now restrict $\hat{\mathbf{x}}$ and $\hat{\mathbf{d}}$ to the quasi-backscattering experimental set-up. In what follows, let $\hat{\mathbf{x}} = -\hat{\mathbf{d}} + \eta\hat{\mathbf{e}}$ where $\eta \in [-\delta,\delta]$ for a small constant δ and $\hat{\mathbf{e}} \in \mathbb{S}^2$ is a fixed unit vector which is orthogonal to $\hat{\mathbf{d}}$. The traditional backscattering set-up corresponds with $\delta = 0$. Using the orthogonality of $\hat{\mathbf{d}}$ with $\hat{\mathbf{e}}$ and the fact that both are unit vectors, a Taylor expansion about $\eta = 0$ yields

$$\hat{\mathbf{x}} = \frac{-\hat{\mathbf{d}} + \eta\hat{\mathbf{e}}}{\left\|-\hat{\mathbf{d}} + \eta\hat{\mathbf{e}}\right\|} = \frac{-\hat{\mathbf{d}} + \eta\hat{\mathbf{e}}}{\sqrt{1+\eta^2}} = -\hat{\mathbf{d}} + \eta\hat{\mathbf{e}} + O(\eta^2).$$

As such, we chose $\hat{\mathbf{x}}$ in this way as an approximation to $\hat{\mathbf{x}} = \frac{-\hat{\mathbf{d}}+\eta\hat{\mathbf{e}}}{\|-\hat{\mathbf{d}}+\eta\hat{\mathbf{e}}\|}$ up to $O(\eta^2)$. For this reason we continue to use the notation $\hat{\mathbf{x}}$, although it is no longer normalized. Substituting this choice of $\hat{\mathbf{x}}$ into (4) gives

$$u_\infty^B(-\hat{\mathbf{d}}+\eta\hat{\mathbf{e}},\hat{\mathbf{d}}) = -\frac{k^2}{4\pi}\int_D e^{2ik\hat{\mathbf{d}}\cdot\mathbf{y}}e^{-ik\eta\hat{\mathbf{e}}\cdot\mathbf{y}}m(\mathbf{y})\,\mathrm{d}\mathbf{y}, \quad \hat{\mathbf{d}}\in\mathbb{S}^1(\hat{\mathbf{e}}) \tag{5}$$

where $\mathbb{S}^1(\hat{\mathbf{e}}) := \{\hat{\mathbf{d}}\in\mathbb{S}^2;\ \hat{\mathbf{d}}\cdot\hat{\mathbf{e}}=0\}$. Following the typical approach of sampling methods in inverse scattering problems, we introduce the quasi-backscattering far field operator, $F : L^2([-\delta,\delta]) \to L^2(\mathbb{S}^1(\hat{\mathbf{e}}))$ which we will use extensively in solving the inverse problem. In particular, F is defined as

$$(Fg)(\hat{\mathbf{d}}) = \int_{-\delta}^{\delta} u_\infty^B(-\hat{\mathbf{d}}+\eta\hat{\mathbf{e}},\hat{\mathbf{d}})g(\eta)\,\mathrm{d}\eta, \qquad \hat{\mathbf{d}}\in\mathbb{S}^1(\hat{\mathbf{e}}). \tag{6}$$

3. Quasi-backscattering inverse problem

We now turn our attention to the inverse problem of reconstructing the location of inhomogeneities from the quasi-backscattering far field data. We first consider the case of obstacles which are small compared to the wavelength of the incident wave and which are sufficiently far from one another. In Section 3.4 , we use the analysis for this case as the basis for finding the centers of extended spherical obstacles. The key result of this section is Theorem 1 which will allow us to locate obstacles by testing if a specific function is in the range of the quasi-backscattering far field operator.

3.1. Inverse problem for small obstacles

Assume there are M obstacles with supports described by $D_j \subset \mathbb{R}^3$, $j = 1,\dots,M$, embedded in a homogeneous background. Let the contrast be defined by the weighted sum of characteristic functions $m(\mathbf{x}) = \sum_{j=1}^M m_j \mathbb{1}_{D_j}$ where m_j are constants.

If $D_j = \mathbf{z}_j + R_j\Omega_j$ are small obstacles centered at a point $\mathbf{z}_j \in \mathbb{R}^3$ with size and shape described by R_j and Ω_j respectively, then using (5) we obtain that up to $O(\max(R_j)^4)$ error terms,

$$u_\infty^B(-\hat{\mathbf{d}}+\eta\hat{\mathbf{e}},\hat{\mathbf{d}}) \simeq \sum_{j=1}^M \tau_j e^{2ik\hat{\mathbf{d}}\cdot\mathbf{z}_j}e^{-ik\eta\mathbf{e}\cdot\mathbf{z}_j},\ \hat{\mathbf{d}}\in\mathbb{S}^1(\hat{\mathbf{e}}),\ \eta\in[-\delta,\delta]. \tag{7}$$

Here, $\tau_j = -\frac{k^2}{4\pi}m_j R_j^3|\Omega_j|$, where $|\Omega_j|$ indicates the volume of Ω_j, are constants related to the strength of each scatterer. Combining (6) and (7) reduces the quasi-backscattering operator to

$$(Fg)(\hat{\mathbf{d}}) = \int_{-\delta}^{\delta} u_\infty^B(-\hat{\mathbf{d}}+\eta\hat{\mathbf{e}},\hat{\mathbf{d}})g(\eta)\,\mathrm{d}\eta = \sum_{j=1}^M \tau_j e^{2ik\hat{\mathbf{d}}\cdot\mathbf{z}_j}\int_{-\delta}^{\delta} e^{-ik\eta\mathbf{e}\cdot\mathbf{z}_j}g(\eta)\,\mathrm{d}\eta.$$

To further simplify the far field operator, we write each obstacle's location in terms of its components parallel to $\hat{\mathbf{e}}$ and perpendicular to $\hat{\mathbf{e}}$. For a fixed $\hat{\mathbf{e}}$, we write $\mathbf{z}_j = \Pi_\perp(\mathbf{z}_j) + L(\mathbf{z_j})\hat{\mathbf{e}}$, $j = 1,\dots,M$ where $\Pi_\perp$ maps onto the plane orthogonal to $\hat{\mathbf{e}}$ and where L isolates the component of a vector which is parallel to $\hat{\mathbf{e}}$. For example, if $\hat{\mathbf{e}} = (0,0,1)$ and $\mathbf{z}_1 = (1,2,3)$, we would have $\Pi_\perp(\mathbf{z}_1) = (1,2,0)$ and $L(\mathbf{z}_1) = 3$. Note that for the sake of conciseness we will sometimes treat $\Pi_\perp(\mathbf{z})$ as a vector in $\mathbb{R}^2$.

Decomposing the locations of obstacles in this way, we can write the far field operator as

$$(Fg)(\hat{\mathbf{d}}) = \sum_{j=1}^{M} \tau_j e^{2ik\hat{\mathbf{d}}\cdot\Pi_\perp(\mathbf{z}_j)} \int_{-\delta}^{\delta} e^{-ikL(\mathbf{z_j})\eta} g(\eta)\,\mathrm{d}\eta. \tag{8}$$

Since F can be computed from the measurable far field pattern data, we use it to solve the inverse scattering problem. Indeed, Theorem 1 gives conditions under which we can relate the range of F to the location of a small obstacle. Such a characterization is typical for sampling-type methods such as the linear sampling or factorization schemes, as well as the MUSIC algorithm. Before stating this theorem, we prove two short lemmas which are required for its proof.

Lemma 1. *Assume $\hat{\mathbf{e}} \in \mathbb{S}^2$ is fixed and let $z_j \in \mathbb{R}^3, j = 1, \ldots, M$ be distinct points whose components in the direction of $\hat{\mathbf{e}}$ differ (i.e., $L(\mathbf{z}_i) \neq L(\mathbf{z}_j), i \neq j$). Then $\mathcal{A} = \{\eta \mapsto e^{-ikL(\mathbf{z}_j)\eta}, j = 1, \ldots, M\}$ is a linearly independent sequences of functions for $\eta \in [-\delta, \delta]$.*

Proof. We would like to show that the Wronskian matrix of $\mathcal{A}$, denoted by W, is non-singular. A short calculation shows that $\det(W) = c(\eta)\det(V)$ where $c(\eta) = \exp\left(-ik\eta\sum_{j=1}^{M} L(\mathbf{z}_j)\right)$ is a function which never vanishes and $V_{(i,j)} = \omega_i^{j-1}$ for $\omega = -ikL(\mathbf{z}_i)$. Since V is a Vandermonde matrix, it has a non-zero determinant so long as $\omega_i \neq \omega_j$ for each $i \neq j$, which is true by the assumption on $L(\mathbf{z}_i), i = 1, \ldots, M$. □

Lemma 2. *Assume $\hat{\mathbf{e}} \in \mathbb{S}^2$ is fixed, let $z_j \in \mathbb{R}^3, j = 1, \ldots, M$ be distinct points, and let $\mathbf{z}_* \in \mathbb{R}^3$ be any point perpendicular to $\hat{\mathbf{e}}$ and distinct from each $\Pi_\perp(z_j)$. Then $\mathcal{B} = \{\hat{\mathbf{d}} \mapsto e^{2ik\hat{\mathbf{d}}\cdot\mathbf{z}}, \mathbf{z} = \mathbf{z}_*, \Pi_\perp(\mathbf{z}_1), \ldots, \Pi_\perp(\mathbf{z}_M)\}$ is a linearly independent sequences of functions for $\hat{\mathbf{d}} \in \mathbb{S}^1(\hat{\mathbf{e}})$.*

The proof of this lemma follows the idea of Theorem 4.1 in [13]. This theorem of Kirsch and Grinberg implies that the above can also be proven for a finite number of $\hat{\mathbf{d}}_j, \eta_j \in \mathbb{S}^1$ with a similar but more technical argument.

Proof. To show that $\mathcal{B}$ is linearly independent, assume

$$\beta_0 e^{2ik\hat{\mathbf{d}}\cdot\mathbf{z}_*} + \sum_{j=1}^{M} \beta_j e^{2ik\hat{\mathbf{d}}\cdot\Pi_\perp(\mathbf{z}_j)} = 0 \quad \text{for} \quad \hat{\mathbf{d}} \in \mathbb{S}^1(\hat{\mathbf{e}}).$$

The left-hand-side of the above equation is, up to a constant multiple, the far field pattern of the function

$$\mathbf{x} \mapsto \beta_0 \Phi(\mathbf{x}, \mathbf{z}_*) + \sum_{j=1}^{M} \beta_j \Phi(\mathbf{x}, \Pi_\perp(\mathbf{z}_j))$$

where

$$\Phi(\mathbf{x}, \mathbf{z}) = \frac{i}{4} H_0^{(1)}(2k|\mathbf{x} - \mathbf{z}|), \qquad \mathbf{x} \neq \mathbf{z} \tag{9}$$

is the (radiating) fundamental solution of the Helmholtz equation in $\mathbb{R}^2$ with wave number $2k$ and $H_0^{(1)}$ is a Hankel function. As such, since the far field pattern vanishes, Rellich's lemma and unique continuation show that

$$\beta_0\Phi(\mathbf{x},\mathbf{z}_*)+\sum_{j=1}^{M}\beta_j\Phi(\mathbf{x},\Pi_\perp(\mathbf{z}_j))=0 \quad \text{for} \quad \mathbf{x}\notin\{\mathbf{z}_*,\Pi_\perp(\mathbf{z}_1),\dots,\Pi_\perp(\mathbf{z}_M)\}.$$

Taking the limit as $\mathbf{x}$ approaches each of $\mathbf{z}_*$ and $\Pi_\perp(\mathbf{z}_j), j=1,\dots,M$ shows immediately that $\mathcal{B}$ is a linearly independent sequence of functions for each $\hat{\mathbf{d}}\in\mathbb{S}^1(\hat{\mathbf{e}})$. □

With these lemmas in hand, we are ready to prove the key theorem for small obstacles.

Theorem 1. *Assume $\hat{\mathbf{e}}\in\mathbb{S}^2$ is fixed and $\hat{\mathbf{d}}\in\mathbb{S}^1(\hat{\mathbf{e}})$. Let $\mathbf{z}_j\in\mathbb{R}^3$ for $j=1,\dots,M$ and let $\mathbf{z}\in\mathbb{R}^3$ be orthogonal to $\hat{\mathbf{e}}$. If the components of each $\mathbf{z}_j$ parallel to $\hat{\mathbf{e}}$ are not equal (i.e., $L(\mathbf{z}_i)\neq L(\mathbf{z}_j), i\neq j$), then $\phi_z(\hat{\mathbf{d}})=e^{2ik\hat{\mathbf{d}}\cdot\mathbf{z}}\in\mathcal{R}(F)$ if and only if $\mathbf{z}\in\{\Pi_\perp(\mathbf{z}_j), j=1,\dots,M\}$.*

Proof. Let $\mathbf{z}\notin\{\Pi_\perp(\mathbf{z}_j), j=1,\dots,M\}$ be orthogonal to $\hat{\mathbf{e}}$. Assume by contradiction that there exists some $g(\eta)\in L^2([-\delta,\delta])$ such that $(Fg)(\hat{\mathbf{d}})=e^{2ik\hat{\mathbf{d}}\cdot\mathbf{z}}$. From the definition of F, this would imply

$$e^{2ik\hat{\mathbf{d}}\cdot\mathbf{z}}=\sum_{j=1}^{M}c_j e^{2ik\hat{\mathbf{d}}\cdot\Pi_\perp(\mathbf{z}_j)},$$

where $c_j=\tau_j\int_{-\delta}^{\delta}e^{-ikL(\mathbf{z}_j)\eta}g(\eta)\,\mathrm{d}\eta$ are constants. However, this is a contradiction with the linear independence of $\{\hat{\mathbf{d}}\mapsto e^{2ik\hat{\mathbf{d}}\cdot\Pi_\perp(\zeta)},\zeta=\mathbf{z},\Pi_\perp(\mathbf{z}_1),\dots,\Pi_\perp(\mathbf{z}_M)\}$, which shows that if $\phi_z\in\mathcal{R}(F)$ then $z\in\{\Pi_\perp(\mathbf{z}_j), j=1,\dots,M\}$.

To prove the second half of the theorem, assume $L(\mathbf{z}_i)\neq L(\mathbf{z}_j)$, $i\neq j$ and $\mathbf{z}\in\{\Pi_\perp(\mathbf{z}_j), j=1,\dots,M\}$. We will show that $\phi_z\in\mathcal{N}(F^*)^\perp=\overline{\mathcal{R}(F)}$ which gives the result since F is a finite rank operator with closed range. A short calculation gives that

$$(F^*h)(\eta)=\sum_{j=1}^{M}\tau_j e^{ikL(\mathbf{z}_j)\eta}\int_{\mathbb{S}^1(\hat{\mathbf{e}})}h(\hat{\mathbf{d}})e^{-2ik\hat{\mathbf{d}}\cdot\Pi_\perp(\mathbf{z}_j)}\,\mathrm{d}s(\hat{\mathbf{d}}).$$

If $h\in\mathcal{N}(F^*)$, then

$$\sum_{j=1}^{M}\tau_j e^{ikL(\mathbf{z}_j)\eta}\int_{\mathbb{S}^1(\hat{\mathbf{e}})}h(\hat{\mathbf{d}})e^{-2ik\hat{\mathbf{d}}\cdot\Pi_\perp(\mathbf{z}_j)}\,\mathrm{d}s(\hat{\mathbf{d}})=0.$$

The linear independence of $\{e^{ikL(\mathbf{z}_j)\eta}, j=1,\dots,M\}$ proven in Lemma 1 gives that for each $j=1,\dots,M$,

$$0=\int_{\mathbb{S}^1(\hat{\mathbf{e}})}h(\hat{\mathbf{d}})e^{-2ik\hat{\mathbf{d}}\cdot\Pi_\perp(\mathbf{z}_j)}\,\mathrm{d}s(\hat{\mathbf{d}})=\Big(h(\hat{\mathbf{d}}),\phi_{\Pi_\perp(\mathbf{z}_j)}(\hat{\mathbf{d}})\Big)_{L^2(\mathbb{S}^1(\hat{\mathbf{e}}))}$$

where $(\cdot,\cdot)_{L^2(\mathbb{S}^1(\hat{\mathbf{e}}))}$ indicates the inner-product on $L^2(\mathbb{S}^1(\hat{\mathbf{e}}))$. As such, $\phi_z\in\mathcal{N}(F^*)^\perp$ for each $\mathbf{z}\in\{\Pi_\perp(\mathbf{z}_j), j=1,\dots,M\}$, which gives the result.

□

The proof of Theorem 1 in fact implies a slightly stronger result.

Corollary 1. *With no restrictions on $L(\mathbf{z}_j)$ and the same hypotheses on $\hat{\mathbf{e}}$ as in Theorem 1, if $\phi_z \in \mathcal{R}(F)$ then $\Pi_\perp(\mathbf{z}) \in \{\Pi_\perp(\mathbf{z}_j), j = 1, \ldots, M\}$.*

Another corollary to Theorem 1 is that, for the appropriate restrictions on $\Pi_\perp(\mathbf{z}_j)$, $P\phi_z = 0$ if and only if $\mathbf{z} \in \{\Pi_\perp(\mathbf{z}_j), j = 1, \ldots, M\}$ where $P : L^2(\mathbb{S}^1(\hat{\mathbf{e}})) \to \mathcal{R}(F)^\perp$ is the orthogonal projection onto the orthogonal complement of the range of F.

This suggests that the function $I(z) = \|P\phi_z\|^{-1}$ for each $\mathbf{z}$ perpendicular to $\hat{\mathbf{e}}$ within a region of interest will be large when $\mathbf{z}$ is near $\Pi_\perp(\mathbf{z}_j), j = 1, \ldots, M$ and small otherwise. This is exactly the MUSIC-type algorithm which we will use to locate the centers of small objects.

To construct the imaging function $I(z)$, let (u_k, σ_k, v_k), $k = 1, 2, \ldots$ be the singular system for F where the left singular functions are $u_k \in L^2(\mathbb{S}^1(\hat{\mathbf{e}}))$ and the right singular functions are $v_k \in L^2([-\delta, \delta])$. Since $\mathcal{R}(F)$ is spanned by the left singular functions u_k which correspond to singular values $\sigma_k = 0$, we can write

$$I(\mathbf{z}) = \left(\sum_{k=r+1}^{\infty} \left| (\phi_z, u_k)_{L^2(\mathbb{S}^1(\hat{\mathbf{e}}))} \right|^2 \right)^{-1}, \tag{10}$$

where r is the number of non-zero singular values. Numerical results showing that $I(\mathbf{z})$ is large near obstacles are given in Section 4.

3.2. A second range test for three-dimensional reconstructions

Assume that the range test described above has been performed so that $\{\Pi_\perp(\mathbf{z}_j), j = 1, \ldots, M\}$ are known. From Theorem 1, $\phi_{\Pi_\perp(\mathbf{z}_k)}(\hat{\mathbf{d}}) \in \mathcal{R}(F)$ for a given $k = 1, \ldots, M$. As such, there is a $g_{\Pi_\perp(\mathbf{z}_k)} \in L^2([-\delta, \delta])$ such that

$$(F g_{\Pi_\perp(\mathbf{z}_k)})(\hat{\mathbf{d}}) = \sum_{j=1}^{M} c_j e^{2ik\hat{\mathbf{d}}\cdot\Pi_\perp(\mathbf{z}_j)} = e^{2ik\hat{\mathbf{d}}\cdot\Pi_\perp(\mathbf{z}_k)}$$

where, as before, $c_j = \tau_j \int_{-\delta}^{\delta} g_{\Pi_\perp(\mathbf{z}_k)}(\eta) e^{-ikL(\mathbf{z}_k)\eta}\, \mathrm{d}\eta$. By linear independence, $c_j = \tau_j \delta_{jk}$, where δ_{jk} is the Kronecker delta function. This suggests a second indicator function which can be used to find $L(\mathbf{z}_j)$ when $\Pi_\perp(\mathbf{z}_j)$ are already known. Formally,

$$J_{\Pi_\perp(\mathbf{z}_k)}(z) = \left(\left| \int_{-\delta}^{\delta} g_{\Pi_\perp(\mathbf{z}_k)}(\eta) e^{-ikL(\mathbf{z})\eta}\, \mathrm{d}\eta \right| \right)^{-1} \tag{11}$$

is arbitrarily large when $z = L(\mathbf{z}_j), j \neq k$. This argument is formal and we have no guarantee that $J_{\Pi_\perp}(\mathbf{z}_k)(z)$ is small away from $\mathbf{z} = \mathbf{z}_j$, $j \neq k$. Nevertheless, in the numerical examples in Section 4.2 below, $J_{\Pi_\perp(\mathbf{z}_k)}$ indicates the location of $L(\mathbf{z}_j)$, as expected when $\Pi_\perp(\mathbf{z}_j)$ are known accurately and $g_z(\eta)$ is calculated using Tikhonov regularization and the Morozov discrepancy principle. As the numerical simulations will demonstrate, however, calculating $L(\mathbf{z}_j)$ in this manner is not robust to noise.

3.3. Inverse problem for coplanar small obstacles

Due to the hypotheses on Theorem 1, the algorithm outlined above does not necessarily locate an object in the case that $L(\mathbf{z}_i) = L(\mathbf{z}_j)$ for some $i \neq j \in 1, \ldots, M$. This problem can be easily alleviated: in all proofs we have assumed a fixed $\hat{\mathbf{e}} \in \mathbb{S}^2$. Since $L(\mathbf{z}_j)$ is a function of $\hat{\mathbf{e}}$, we can perform multiple quasi-backscattering experiments

with different $\hat{\mathbf{e}}$ directions to solve the problem. Indeed, we recommend this for purely geometric reasons as well. Since the quasi-backscattering technique gives only two-dimensional projections of the locations of scatterers, two obstacles which lie on top of each other with respect to $\hat{\mathbf{e}}$ (i.e., $\Pi_\perp(\mathbf{z}_i) = \Pi_\perp(\mathbf{z}_j)$ but $L(\mathbf{z}_i) \neq L(\mathbf{z}_j)$) will appear as the same obstacle in the reconstruction. Multiple experiments corresponding to different $\hat{\mathbf{e}}$ directions helps to fix this problem as well. In Section 4.3, we outline a technique for using data from multiple experiments with different $\hat{\mathbf{e}}$ directions to reconstruct obstacles in three-dimensions.

Before continuing, we note that the algorithm outlined above does not necessarily identify obstacles if $L(\mathbf{z}_i) = L(\mathbf{z}_j)$ for all $i \neq j$. In particular, under these conditions, we show below that there is no obvious reason which suggests that $I(\mathbf{z})$ will be arbitrarily large at $\mathbf{z} = \Pi_\perp(\mathbf{z}_j)$, $j = 1, \ldots, M$. Indeed, the numerical simulations in Section 4 indicate that the reconstruction of co-planar obstacles is sensitive to noise.

Assume that $L(\mathbf{z}_i) = L(\mathbf{z}_j)$ for each $i, j = 1, \ldots, M$. Since we can shift the origin with a change of variables, we set each $L(\mathbf{z}_i) = 0$ without loss of generality. In this case, the far field operator becomes

$$(Fg)(\hat{\mathbf{d}}) = \sum_{j=1}^{M} \tau_j e^{2ik\hat{\mathbf{d}}\cdot\Pi_\perp(\mathbf{z}_j)} \int_{-\delta}^{\delta} g(\eta)\, \mathrm{d}\eta, \quad \hat{\mathbf{d}} \in \mathbb{S}^1(\hat{\mathbf{e}}),$$

and Fubini's Theorem gives that for $\eta \in [-\delta, \delta]$,

$$(F^*h)(\eta) = \sum_{j=1}^{M} \tau_j \int_{\mathbb{S}^1(\hat{\mathbf{e}})} e^{-2ik\hat{\mathbf{d}}\cdot\Pi_\perp(\mathbf{z}_j)} h(\hat{\mathbf{d}})\, \mathrm{d}s(\hat{\mathbf{d}}) = \left(h(\hat{\mathbf{d}}), \sum_{j=1}^{M} \tau_j \phi_{\Pi_\perp(\mathbf{z}_j)} \right)_{L^2(\mathbb{S}^1(\hat{\mathbf{e}}))}.$$

Let $h(\hat{\mathbf{d}}) = u_k(\hat{\mathbf{d}})$ for a fixed k where $u_k(\hat{\mathbf{d}})$ is a left singular function of F corresponding to a singular value $\sigma_k = 0$. Since $u_k \in \mathcal{N}(F^*)$,

$$\left(u_k(\hat{\mathbf{d}}), \sum_{j=1}^{M} \tau_j \phi_{\Pi_\perp(\mathbf{z}_j)} \right)_{L^2(\mathbb{S}^1(\hat{\mathbf{e}}))} = (F^*u_k)(\eta) = 0.$$

However, we cannot conclude from the above equation that

$$\left(u_k(\hat{\mathbf{d}}), \phi_{\Pi_\perp(\mathbf{z}_j)} \right)_{L^2(\mathbb{S}^1(\hat{\mathbf{e}}))} = 0, \qquad j = 1, \ldots, M.$$

3.4. Inverse problem for extended obstacles

We now adapt the arguments given in the previous section to the problem of finding extended obstacles. We show that, for small δ, the arguments given in Theorem 1 apply directly to locating the center of extended spherical obstacles. While the spherical nature of the extended obstacles does not seem to be required, it is not clear that we can uncover more information than the location of the center of these obstacles.

In this section, assume there are M obstacles D_j again of the form $D_j = \mathbf{z}_j + R_j\Omega_j$, where $\mathbf{z}_j$ are the obstacles' center, Ω_j their shape, and R_j their size. Now, however, assume each $\Omega_j = B(0;1)$ is a ball centered at zero of radius one and that R_j is of similar size as the wavelength or larger. Assume, as before, that the contrast is

defined by $m = \sum_{j=1}^{M} m_j \mathbb{1}_{D_j}$ where m_j are constants. We will begin our discussion by calculating $u_\infty^B(\hat{\mathbf{x}}, \hat{\mathbf{d}})$ under these assumptions. From (4) we have

$$\begin{aligned} u_\infty^B(\hat{\mathbf{x}}, \hat{\mathbf{d}}) &= -\frac{k^2}{4\pi} \sum_{j=1}^{M} m_j \int_{D_j} e^{ik(\hat{\mathbf{d}}-\hat{\mathbf{x}})\cdot\mathbf{y}} \, \mathrm{d}\mathbf{y} \\ &= -\frac{k^2}{4\pi} \sum_{j=1}^{M} m_j e^{ik(\hat{\mathbf{d}}-\hat{\mathbf{x}})\cdot\mathbf{z}_j} \int_{B(\mathbf{0};R_j)} e^{ik(\hat{\mathbf{d}}-\hat{\mathbf{x}})\cdot\mathbf{y}} \, \mathrm{d}\mathbf{y}. \end{aligned}$$

To simplify this expression into a more useful one, we state the following lemma.

Lemma 3. *For a constant $R > 0$ and any two vectors $\mathbf{x}, \mathbf{y} \in \mathbb{R}^3$,*

$$\int_{B(\mathbf{0};R)} e^{i\mathbf{x}\cdot\mathbf{y}} \, \mathrm{d}\mathbf{y} = \frac{4\pi}{|\mathbf{x}|^3} \left(\sin(R|\mathbf{x}|) - R|\mathbf{x}| \cos(R|\mathbf{x}|) \right).$$

Proof. Under the change of coordinates $\mathbf{y} \mapsto r\hat{\mathbf{y}}$ where $r = |\mathbf{y}|$,

$$\int_{B(\mathbf{0};R)} e^{i\mathbf{x}\cdot\mathbf{y}} \, \mathrm{d}\mathbf{y} = \int_0^R r^2 \int_{\mathbb{S}^2} e^{ir\mathbf{x}\cdot\hat{\mathbf{y}}} \, \mathrm{d}s(\hat{\mathbf{y}}) \, \mathrm{d}r. \tag{12}$$

It is known that $\int_{\mathbb{S}^2} e^{ir\mathbf{x}\cdot\hat{\mathbf{y}}} \, \mathrm{d}s(\hat{\mathbf{y}}) = 4\pi j_0(r\mathbf{x})$ where j_0 is the spherical Bessel function of order zero [14]. Since $j_0(x) = \frac{\sin(x)}{x}$, an integration-by-parts gives the result. □

We are interested in the above result for $\mathbf{x} = k(\hat{\mathbf{d}} - \hat{\mathbf{x}})$ and $R = R_j$. With this choice of parameters,

$$u_\infty^B(\hat{\mathbf{x}}, \hat{\mathbf{d}}) = -k^2 \sum_{j=1}^{M} m_j e^{ik(\hat{\mathbf{d}}-\hat{\mathbf{x}})\cdot\mathbf{z}_j} \left(\frac{\sin(kR_j|\hat{\mathbf{d}} - \hat{\mathbf{x}}|) - kR_j|\hat{\mathbf{d}} - \hat{\mathbf{x}}| \cos(kR_j|\hat{\mathbf{d}} - \hat{\mathbf{x}}|)}{(k|\hat{\mathbf{d}} - \hat{\mathbf{x}}|)^3} \right).$$

Returning to the quasi-backscattering approach and letting $\hat{\mathbf{x}} = -\hat{\mathbf{d}} + \hat{\mathbf{e}}\eta$, a Taylor expansion about $\eta = 0$ gives that

$$\frac{\sin(kR_j|\hat{\mathbf{d}} - \hat{\mathbf{x}}|) - kR_j|\hat{\mathbf{d}} - \hat{\mathbf{x}}| \cos(kR_j|\hat{\mathbf{d}} - \hat{\mathbf{x}}|)}{(k|\hat{\mathbf{d}} - \hat{\mathbf{x}}|)^3} = \frac{\sin(2kR_j) - 2kR_j \cos(2kR_j)}{(2k)^3} + O(\eta^2), \quad j = 1, \ldots, M.$$

If we again define the quasi-backscattering far field operator as $(Fg)(\hat{\mathbf{d}}) = \int_{-\delta}^{\delta} u_\infty^B(\hat{\mathbf{d}}, \eta) g(\eta) \, \mathrm{d}\eta$, we find

$$\begin{aligned} (Fg)(\hat{\mathbf{d}}) &= \sum_{j=1}^{M} \tau_j^L e^{2ik\hat{\mathbf{d}}\cdot\mathbf{z}_j} \left(\int_{-\delta}^{\delta} e^{-ik\eta\hat{\mathbf{e}}\cdot\mathbf{z}_j} g(\eta) \, \mathrm{d}\eta + o(\delta^2) \right) \\ &= \sum_{j=1}^{M} \tau_j^L e^{2ik\hat{\mathbf{d}}\cdot\Pi_\perp(\mathbf{z}_j)} \left(\int_{-\delta}^{\delta} e^{-ikL(\mathbf{z_j})\eta} g(\eta) \, \mathrm{d}\eta + o(\delta^2) \right) \end{aligned}$$

where $\tau_j^L = -m_j(\sin(2kR_j) - 2kR_j \cos(2kR_j))/8k$. Here, the asymptotic analysis follows from an application of Cauchy-Schwarz. Up to constants and $o(\delta^2)$, the quasi-backscattering operator for extended spheres is identical to (8), the quasi-backscattering operator for small obstacles. As such, using the same technique described in Section 3.1, we can find two-dimensional projections of the centers of extended spherical obstacles. Note, incidentally, that $\tau_j^L = -\frac{1}{3}k^2 m_j R_j^3 + O(R_j^5)$, which matches the expression for τ_j used in the case of small spheres.

4. Numerical experiments

In this section, we give numerical results demonstrating the effectiveness of the above technique. In all experiments, we approximate obstacles by spheres with a small radius. Specifically, the radius for each obstacle is 1/500 units. We will use simulated forward data which is corrupted by random noise. Using the formula given in (4) we simulate $u_\infty(\hat{\mathbf{x}}, \hat{\mathbf{d}})$ using numerical integration. Numerically integrating (6) gives a discrete representation of the far field matrix, F_{ij}, which is corrupted by $F_{ij}(1 + \gamma\xi)$ where ξ is a uniform random variable in $[-1, 1]$ and γ is a constant related to the level of noise. To calculate the indicator function, we compute the singular value decomposition of $F = USV^*$ and use U to calculate a discrete version of (10). The approximate imaging function is regularized by computing with all but the first ten singular vectors (i.e., $r = 9$ in (10)). In all examples, we take $k = 15$ to be the wave number. Other parameters are given for each experiment.

The experimental parameters discussed above merit a few comments. The first is related to our use of ten singular vectors in reconstructions. Typically when using a MUSIC-type algorithm, the number of singular vectors is related to the number of unknown obstacles, which is estimated by the numerical rank of the far field operator. In our numerical experiments we have found such a technique to be sensitive to added noise. As such, we took the number of singular vectors as an upper bound of the number of obstacles. This method for picking the number of singular values could result in false positives in reconstructions; though seemingly unlikely in practice, there is no guarantee that this modification of the indicator function in (10) will be large only at obstacle locations. A more robust technique for picking the number of singular vectors would be useful in practice. Nevertheless, in the experiments below, results do not change noticeably when using the same number of singular vectors as there are obstacles.

The second comment is related to the relatively-high wave number used in these experiments. In the case of extended obstacles, low wave numbers are used to ensure that the Born approximation of the far field is valid. However, because we assume our objects are very small (a radius of 1/500 units), we are justified in using a higher wave number.

We present three types of numerical inversions. In Section 4.1, we show two-dimensional projections of small obstacles. In Section 4.2, we generate the third unknown coordinate assuming the first two are known. Finally, we use multiple $\hat{\mathbf{e}}$-directions to generate full three-dimensional reconstructions for small obstacles in Section 4.3.

4.1. Two-dimensional projections of small obstacles

We give several numerical examples in this section which help demonstrate both the strengths and weaknesses of the quasi-backscattering technique. In all reconstructions, darker colors correspond to higher values of the imaging function which correspond with the predicted locations of the obstacles. A small red circle in each picture corresponds to the true location of each obstacle. Note that the size of the dark areas near obstacle locations do not correspond to an estimate of obstacle size, but are merely an artifact of the way in which reconstructions are displayed. In all reconstructions, we use 80^2 sampling points uniformly chosen in the unit-square. In all experiments we use 95 incident directions and for each incident direction we use 95 locations for

$\hat{\mathbf{x}}$ between $-\delta$ and δ. We call these points between $-\delta$ and δ the observation points. This is a large number of both incident directions and observation points and, indeed, acceptable results are achievable with far fewer. However, we prefer to focus these experiments on the affect geometric and physical parameters have on reconstructions.

The first example, given in Figures 2 and 3, shows the algorithm differentiating between multiple small obstacles, added one at a time. The obstacles are located at $\mathbf{z}_1 = (-0.25, -0.25, -0.5)$, $\mathbf{z}_2 = (0.25, 0.25, -0.25)$, $\mathbf{z}_3 = (0.25, -0.25, 0.25)$, and $\mathbf{z}_4 = (-0.25, 0.25, 0.5)$.

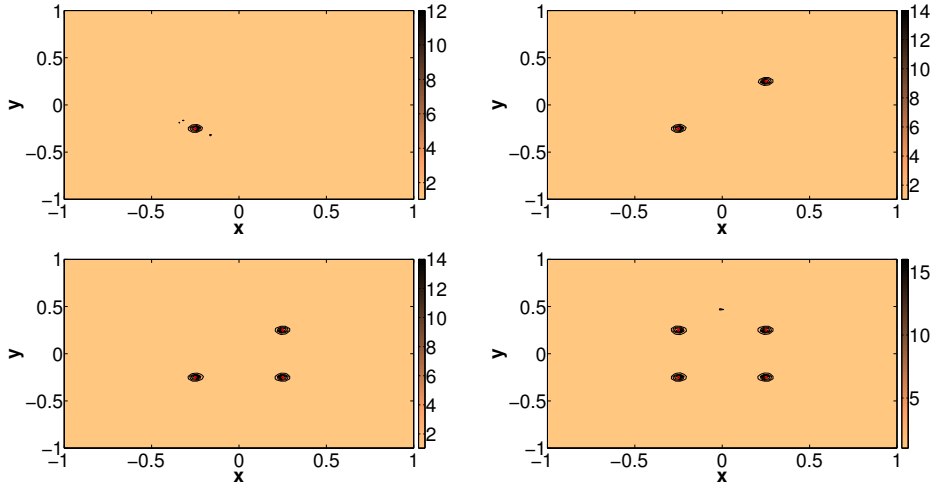

Figure 2: Symmetric addition of new objects, $\delta = \pi/50$ (no noise).

For the next example, we show the affect of δ on reconstructions. While the motivation for the quasi-backscattering set-up comes from a Taylor expansion about $\eta = 0$ (and hence small δ), the experiments in Figure 4 show that in the presence of noise, the reconstruction technique is not stable for too small of δ, in particular when many obstacles are present. All three figures have $\mathbf{z}_1 = (0, -0.5, 0.25)$, $\mathbf{z}_2 = (0, 0.5, -0.75)$, $\mathbf{z}_3 = (0.5, 0, -0.25)$, and $\mathbf{z}_4 = (-0.5, 0, 0.75)$.

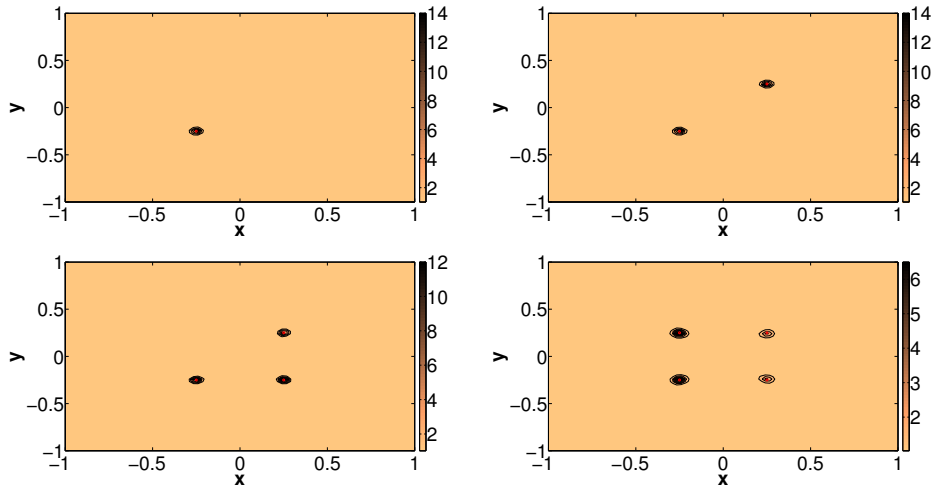

Figure 3: Symmetric addition of new objects, $\delta = \pi/50$ (approximately 1% noise).

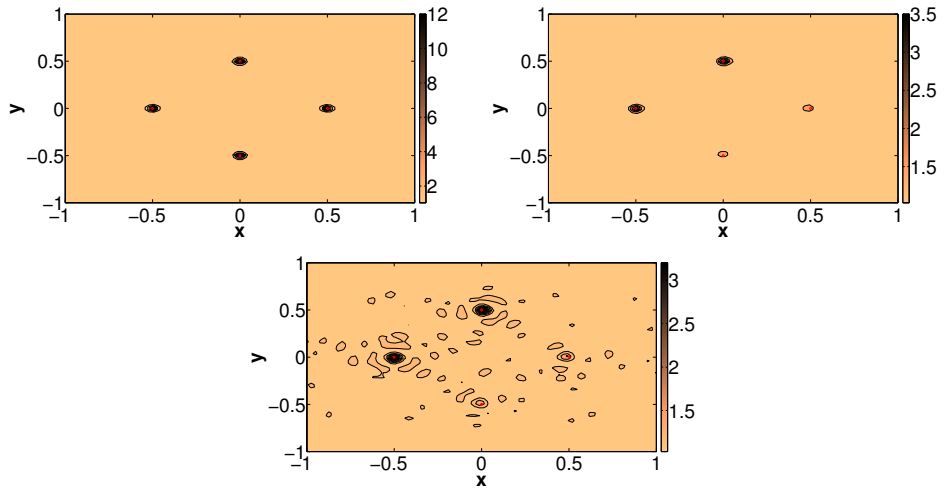

Figure 4: Decreasing the quasi-parameter δ. Figures have $\delta = \pi$ (top-left), $\delta = \pi/50$ (top-right), and $\delta = \pi/100$ (bottom). Approximately 5% noise.

In the experiment in Figure 5 we show the resolution achievable by the quasi-backscattering technique. Often, inversion schemes based on the Born approximation or a Fourier transform are limited to a half-wavelength resolution. Though we do not show this rigorously, the numerical example in Figure 5 suggests such a limitation for the quasi-backscattering technique. Indeed, we see that the method is unable to differentiate between obstacles once they are within half a wavelength of each other. In this case, the technique gives a large range of possible locations, containing the true centers of the obstacles. In this experiment, there is a constant 0.2 unit distance between the z-coordinate of the obstacles.

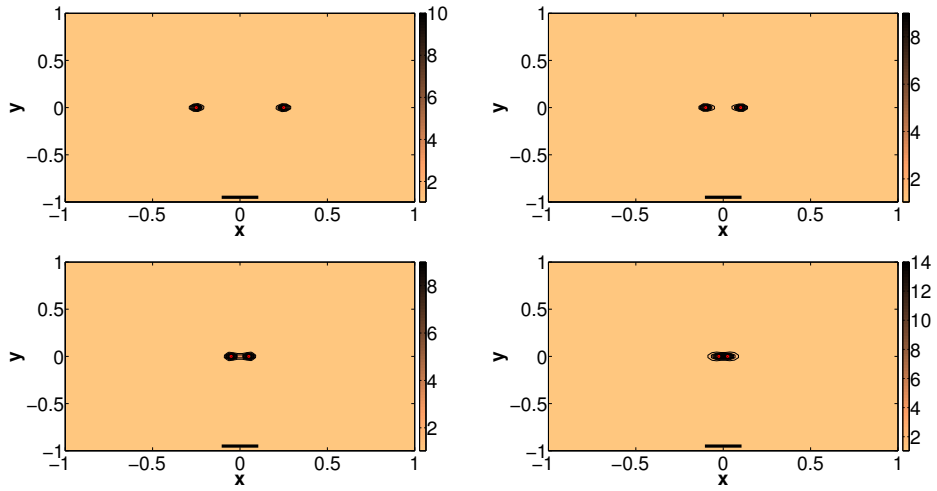

Figure 5: Two objects moving closer to each other, $\delta = \pi/100$ (no noise). Thick bar at bottom corresponds to half of wavelength.

The final two experiments of this type show the need to take multiple experiments with different $\hat{\mathbf{e}}$ directions when the underlying geometry of the obstacles is complicated. Figure 10 shows reconstructions from three different $\hat{\mathbf{e}}$ directions of three small obstacles which would form an approximate "L"-shape if they were connected with straight lines. In particular, $\mathbf{z}_1 = (-0.25, -0.25, -0.25)$, $\mathbf{z}_2 = (0.25, -0.24, -0.25)$, and $\mathbf{z}_3 = (-0.25, -0.26, 0.25)$. Due to the geometry of the obstacles, taking $\hat{\mathbf{e}} = (0, 0, 1)$ or $\hat{\mathbf{e}} = (1, 0, 0)$ only gives reconstructions of two of the three obstacles. By taking $\hat{\mathbf{e}} = (0, 1, 0)$, however, we are able to find all three obstacles.

Finally, we apply the quasi-backscattering algorithm to the reconstruction of coplanar obstacles – that is, obstacles which violate the assumptions in Theorem 1. As Figure 11 shows, in the absence of noise, reconstructions are acceptable. However, under the addition of noise, the reconstructions become less clean. Changing $\hat{\mathbf{e}}$ so that $L(\mathbf{z}_i) \neq L(\mathbf{z}_j)$ results in more acceptable reconstructions. The figures are located at $\mathbf{z}_1 = (0.75, 0.75, 0.25)$ and $\mathbf{z}_2 = (-0.25, -0.25, 0.25)$.

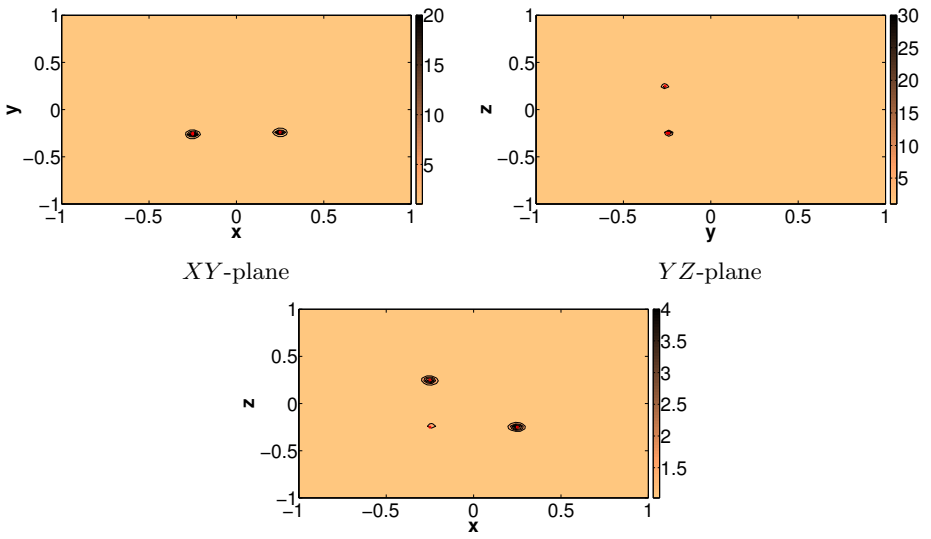

XY-plane YZ-plane

XZ-plane

Figure 10: An L-Shaped geometry which requires 3 views to see all obstacles, $\delta = \pi/30$ (approximately 1% noise).

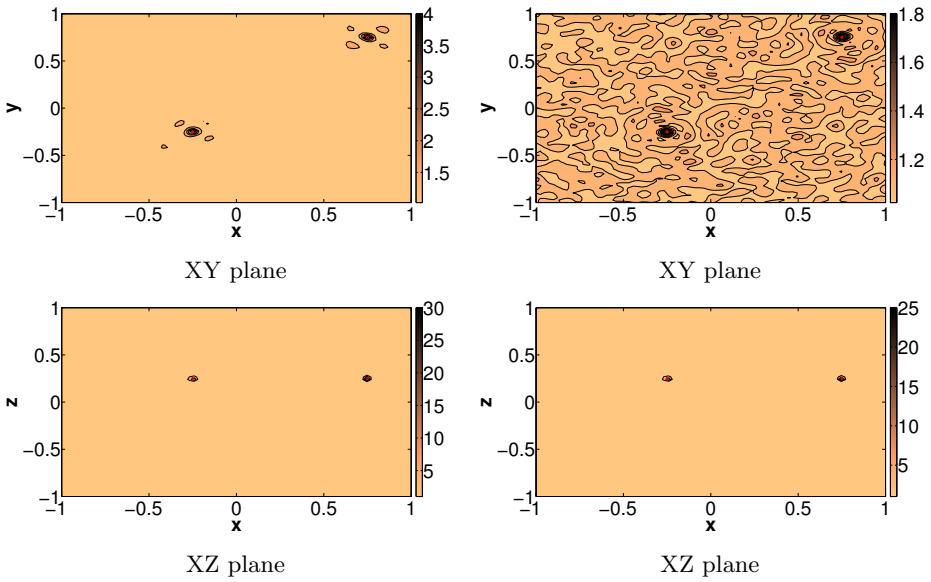

XY plane XY plane

XZ plane XZ plane

Figure 11: Results for co-planar obstacles, $\delta = \pi/60$. Figures on left are noise-free and figures on right have approximately 1% noise.

4.2. Reconstruction of third coordinate

We now show two reconstructions of the third coordinate of a small obstacle, assuming the other two coordinates are known. We use the indicator function given by (11)

where $g_z(\eta)$ is calculated using Tikhonov regularization plus the Morozov discrepancy principle. In both reconstructions, we take $\delta = \pi/50$ and 377 observation points and incident directions. Though this is an unrealistically-large number of observation points and incident directions, we will show that the indicator function is still sensitive to noise. In both reconstructions, $\hat{\mathbf{e}} = (0, 0, 1)$ so that we are generating the z-coordinate in a typical Cartesian plane. For this reason, we explore another technique for three-dimensional reconstructions in Section 4.3 below.

In Figure 12, let $\mathbf{z}_1 = (-0.24, -0.24, -0.75)$, $\mathbf{z}_2 = (0.26, -0.24, 0)$, and $\mathbf{z}_3 = (0.26, 0.26, 0.75)$. Adding no noise and assuming the two-dimensional projections of $\mathbf{z}_j, j = 1, 2, 3$ are known exactly, the figure demonstrates we are able to construct $L(\mathbf{z}_j)$ under ideal circumstances.

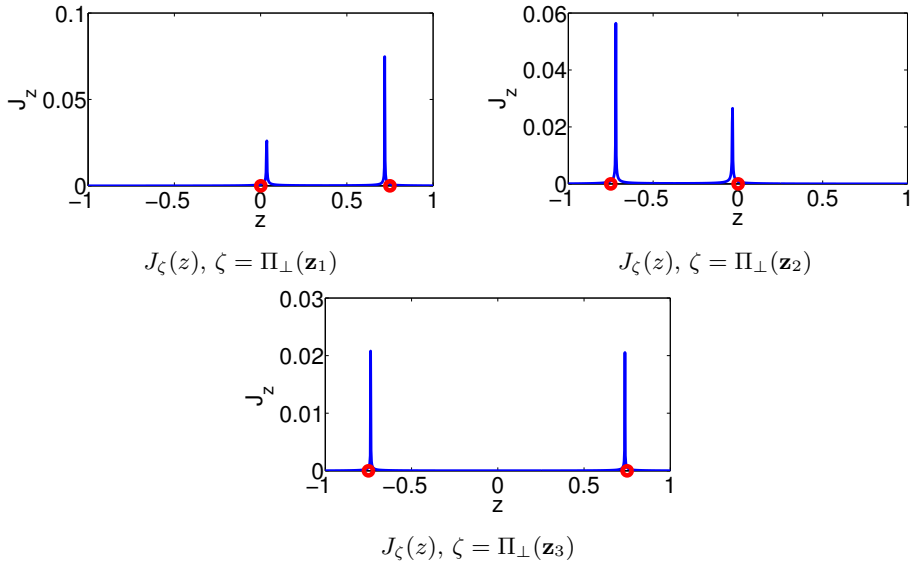

$J_\zeta(z)$, $\zeta = \Pi_\perp(\mathbf{z}_1)$

$J_\zeta(z)$, $\zeta = \Pi_\perp(\mathbf{z}_2)$

$J_\zeta(z)$, $\zeta = \Pi_\perp(\mathbf{z}_3)$

Figure 12: When $J_{\Pi_\perp(\mathbf{z}_j)}$ is computed, peaks appear for $i \neq j$. Red circles show exact location of $L(\mathbf{z}_j)$.

We consider a more realistic scenario in Figure 13. Let $\mathbf{z}_1 = (-0.25, -0.25, -0.75)$, $\mathbf{z}_2 = (0.25, -0.25, 0)$, and $\mathbf{z}_3 = (0.25, 0.25, 0.75)$. However, we have added 0.1% noise and assume we guess $\Pi_\perp(\mathbf{z}_1) = (-0.24, -0.24)$, $\Pi_\perp(\mathbf{z}_2) = (0.26, -0.24)$, and $\Pi_\perp(\mathbf{z}_3) = (0.26, 0.26)$. We see that even under small perturbations, the accuracy of the reconstructions is dramatically decreased.

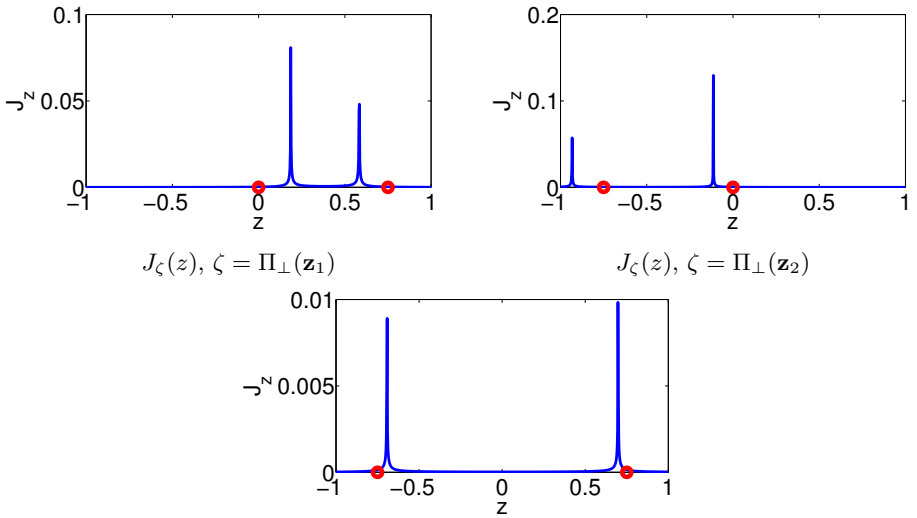

$J_\zeta(z)$, $\zeta = \Pi_\perp(\mathbf{z}_1)$ $J_\zeta(z)$, $\zeta = \Pi_\perp(\mathbf{z}_2)$

$J_\zeta(z)$, $\zeta = \Pi_\perp(\mathbf{z}_3)$

Figure 13: Reconstructions lose accuracy in the presence of 0.1% noise. Red circles show exact location of $L(\mathbf{z}_j)$.

4.3. Three-dimensional reconstructions

The inversion schemes described above do a good job locating obstacles within the two-dimensional plane perpendicular to the selected $\hat{\mathbf{e}}$ direction. Given data from multiple experiments with multiple $\hat{\mathbf{e}}$ directions, we are better able to find the full three-dimensional coordinates of an obstacle or set of obstacles. As discussed above, there are many scenarios in which reconstructing obstacles with multiple $\hat{\mathbf{e}}$ is encouraged. In this section, we show that multiple $\hat{\mathbf{e}}$ directions can be used to calculate three-dimensional reconstructions of obstacle locations.

The creation of three-dimensional images from a selection of two-dimensional projections has been thoroughly studied in the image processing literature and we do not attempt to use state-of-the-art techniques here. Instead, we perform multiple quasi-backscattering experiments on the same obstacle set-up, interpolate the results from each experiment onto a fixed sampling grid, and average the results. We regularize our results for each $\hat{\mathbf{e}}$ before computing the averaged result. In particular, we apply a total variation minimization algorithm (see [4, 5, 15]) which emphasizes changes in gradient and hence sharpens edges. We next locally normalize each two-dimensional projection over a 5×5 grid of sampling points to further sharpen edges. After these regularization steps are performed, we average on a sampling grid as described.

We compute forward and inverse data for this section as we did in Section 3.1. Here, however, we vary $\hat{\mathbf{e}}$. Specifically, we take 30 values of $\hat{\mathbf{e}}$ from a circle in the XY-plane. The results are given as three-dimensional contour plots of the imaging function. The contour which is plotted is $\alpha \max I(z)$ where α is a value between 0 and 1.

In Figure 14, we demonstrate the techniques described above to compute three-dimensional object reconstructions. In particular, we consider three small objects

located at the points $\mathbf{z}_1 = (-0.5, -0.5, -0, 5)$, $\mathbf{z}_2 = (0.5, -0.5, -0.5)$, and $\mathbf{z}_3 = (-0.5, -0.5, 0.5)$. Notice that these are in a geometry which forms an "L"-shape, as in Figure 11. As demonstrated above, when we use two-dimensional projection techniques, we require at least three $\hat{\mathbf{e}}$ directions to locate all objects for such a geometry. By taking more $\hat{\mathbf{e}}$ directions, however, we are able to give a full three-dimensional image of the geometry.

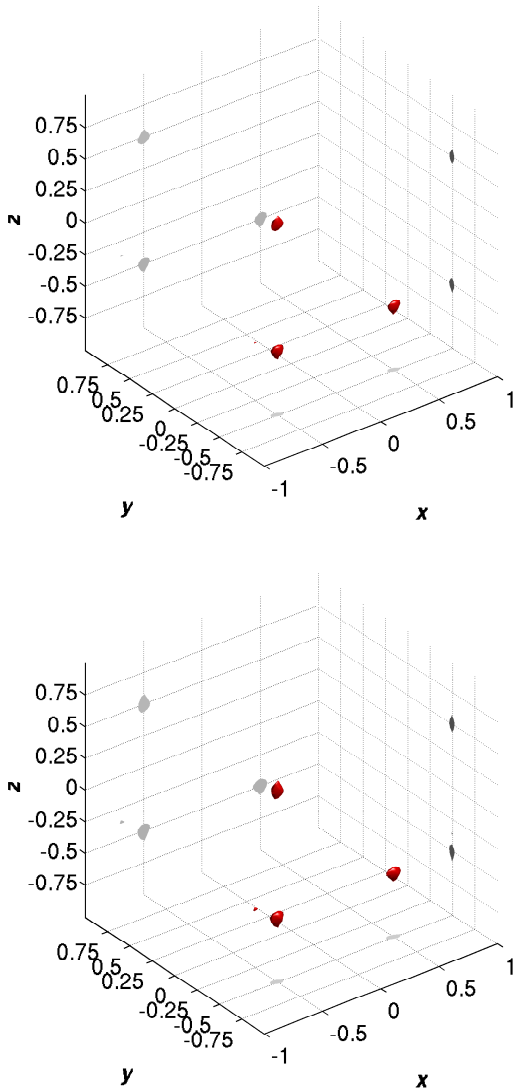

Figure 14: Three-dimensional noise-free reconstructions of point obstacles based on multiple experiments. We take 95 incident directions, 95 observation points, and use $\delta = \pi/60$. The top figure is noise-free while the bottom figure has approximately 1% noise. In both figures, we display isovalues of 0.6 times the maximum value of the imaging function.

Acknowledgement

This research was initiated while JDR was visiting École Polytechnique where he was supported by INRIA-DeFI. The hospitality of that institution is gratefully acknowledged. Fioralba Cakoni is also thanked for her many helpful suggestions.

References

[1] H. Ammari, E. Iakovleva and D.Lesselier. *Two numerical methods for recovering small inclusion from the scattering amplitude at a fixed frequency.* SIAM J. Sci. Comput, 27 (2005), pp. 130-158.

[2] H. Ammari and H. Kang. *Reconstruction of small inhomogeneities from boundary measurements*, volume 1846 of *Lecture Notes in Mathematics*. Springer-Verlag, Berlin, 2004.

[3] F. Cakoni & D. Colton, *A Qualitative Approach to Inverse Scattering Theory.* Springer, New York NY (2014).

[4] A. Chambolle, *An algorithm for total variation minimization and applications.* Journal of Mathematical Imaging and Vision **20**, pp 89-97 (2004).

[5] A. Chambolle & T. Pock, *A first-order primal-dual algorithm for convex problems with applications to imaging.* Journal of Mathematical Imaging and Vision **40**, pp 120-145 (2010).

[6] D. Colton, H. Haddar, and M. Piana. *The linear sampling method in inverse electromagnetic scattering theory. Inverse Problems*, 19(6):S105–S137, 2003. Special section on imaging.

[7] D. Colton & R. Kress, *Inverse Acoustic and Electromagnetic Scattering Theory*, Third Edition. Springer, New York NY (2013).

[8] M. Cheney, *The linear sampling method and the MUSIC algorithm.* Inverse Problems **17**, pp 591-595 (2001).

[9] F. Collino, M'B. Fares & H. Haddar. *Numerical and analytical studies of the linear sampling method in electromagnetic inverse scattering problems. Inverse Problems*, 19(6):1279–1298, 2003.

[10] A.J. Devaney, *Super-resolution processing of multi-static data using time reversal and MUSIC.* Unpublished paper, preprint available on the author's website (2000).

[11] H. Haddar & R. Mdimagh *Identification of small inclusions from multistatic data using the reciprocity gap concept* Inverse Problems, 2012, 28 (4), pp.045011, 19.

[12] A. Kirsch. *The MUSIC algorithm and the factorization method in inverse scattering theory for inhomogeneous media.* Inverse Problems, 18(4):1025–1040, 2002.

[13] A. Kirsch and N. Grinberg, *The Factorization Method for Inverse Problems.* Clarendon Press, Oxford UK (2008).

[14] P. Martin, *Multiple Scattering: Interaction of Time-Harmonic Waves with N Obstacles.* Cambridge University Press, Cambridge UK (2006).

[15] L. Rudin, S.J. Osher, & E. Fatemi. *Nonlinear total variation based noise removal algorithms.* Physica D **60**, pp 259-268 (1992).